Enhancement of Lamina Cribrosa Visibility in Optical Coherence Tomography Images Using Adaptive Compensation

Jean Martial Mari,[1] *Nicholas G. Strouthidis,*[2,3] *Sung Chul Park,*[4,5] *and Michaël J. A. Girard*[3,6,7]

Purpose. We improved the visibility of the lamina cribrosa (LC), including its posterior boundary, in optical coherence tomography (OCT) images of the human optic nerve head (ONH).

Methods. An adaptive compensation algorithm was developed to overcome a limitation of our standard compensation algorithm, that is the overamplification of noise at high depth. Such limitation currently hampers our ability to distinguish the posterior LC boundary. In adaptive compensation, standard compensation operations are performed until an energy threshold is reached, at which stage the compensation process is stopped to limit noise overamplification in the deeper portion of the OCT image. The performance of adaptive compensation was compared to that of standard compensation using OCT images of 5 human ONHs.

Results. Adaptive compensation significantly reduced the intralayer contrast (a measure of pixel intensity uniformity) in the deeper portion of the OCT images (from 0.62 ± 0.11–0.30 ± 0.03, $P < 0.001$), indicating successful removal of noise overamplification. Furthermore, adaptive compensation significantly increased the interlayer contrast (a measure of boundary visibility) across the posterior LC boundary (from 0.29 ± 0.13–0.61 ± 0.21, $P < 0.001$), indicating improved posterior LC boundary visibility.

Conclusions. Adaptive compensation provided significant improvement compared to standard compensation by eliminating noise overamplification at high depth and improving the visibility of the posterior LC boundary. These improvements were performed while maintaining all other benefits of compensation, such as shadow removal and contrast enhancement. Adaptive compensation will help further our efforts to characterize in vivo ONH biomechanics for the diagnosis and monitoring of glaucoma. (*Invest Ophthalmol Vis Sci.* 2013; 54:2238–2247) DOI:10.1167/iovs.12-11327

Optical coherence tomography (OCT) is a noninvasive imaging modality that has a number of applications in clinical ophthalmology, particularly for the assessment of macular pathology, anterior segment anatomy, and glaucoma. Until recently, OCT imaging in optic neuropathies, including glaucoma, has focused on the measurement of retinal nerve fiber layer thickness in the peripapillary region. With the introduction of spectral domain and swept source OCT technology, improvements in axial resolution as well as increased A-Scan acquisition rates have enabled the visualization of structures deep to the surface of the optic nerve head (ONH), such as the lamina cribrosa (LC).[1–10] The LC is a porous connective tissue through which retinal ganglion cell axon bundles pass in transit to the orbital portion of the optic nerve. The LC appears to be of central importance in many optic neuropathies, such as glaucoma,[11–15] papilledema,[16–18] and anterior ischemic optic neuropathy.[19,20] The LC serves as a location where nerve bundles are "vulnerable" to injury, whether this is due to direct mechanical stress, secondary to compromise in the local blood supply, or through local interruption in axoplasmic flow. An ability to image the three-dimensional structure of the LC accurately, as should be possible using spectral domain OCT, will have clinical applications in assisting in the diagnosis of, and in risk-profiling for, these optic neuropathies. Unfortunately, our ability to visualize the full "depth" of the LC is limited. This is due to light attenuation, whereby signal strength diminishes as a function of depth.[10,21] This optical phenomenon is an important barrier to the clinical application of LC imaging, as visualization of the LC remains highly variable using current OCT technologies. This phenomenon impacts upon all currently available clinical devices, and varies from eye to eye with some eyes (particularly eyes with large cups and "thinner" prelaminar tissues) being less affected by signal attenuation than eyes with smaller cups and "thicker" prelaminar tissues.

We recently have proposed a postprocessing compensation method to improve the quality of OCT images by correcting the deleterious effects of light attenuation. When applied to images of the ONH, our technique was shown to remove blood vessel shadows cast by the central retinal vessel trunk and drastically improve the visibility of the full width of the anterior LC surface.[10] In some instances the methodology could improve the visualization of LC insertions and LC defects. When applied to images of arterial tissue, our compensation

From [1]INSERM 1032, Université de Lyon, Lyon, France; the [2]NIHR Biomedical Research Centre, Moorfields Eye Hospital NHS Foundation Trust & UCL Institute of Ophthalmology, London, United Kingdom; the [3]Singapore Eye Research Institute, Singapore National Eye Centre, Singapore; [4]Moise and Chella Safra Advanced Ocular Imaging Laboratory, Einhorn Clinical Research Center, New York Eye and Ear Infirmary, New York, New York; the [5]Department of Ophthalmology, New York Medical College, Valhalla, New York; the [6]In Vivo Biomechanics Laboratory, Department of Bioengineering, National University of Singapore, Singapore; and the [7]Department of Ophthalmology, Yong Loo Lin School of Medicine, National University of Singapore, Singapore.

Supported by Singapore Ministry of Education Academic Research Fund Tier 1 (MJAG), and by the Department of Health through the award made by the National Institute for Health Research to Moorfields Eye Hospital NHS Foundation Trust and UCL Institute of Ophthalmology for a Biomedical Research Centre for Ophthalmology. The authors alone are responsible for the content and writing of the paper.

Submitted for publication November 19, 2012; revised January 23, 2013; accepted February 18, 2013.

Disclosure: **J.M. Mari**, None; **N.G. Strouthidis**, None; **S.C. Park**, None; **M.J.A. Girard**, None

Corresponding author: Michaël J. A. Girard, In Vivo Biomechanics Laboratory, Department of Bioengineering, National University of Singapore, 9 Engineering Drive 1, Block EA #03-12, Singapore 117576; mgirard@nus.edu.sg.

technique improved successfully the visibility of coronary artery plaques.[21] While such a compensation technique can provide important enhancements that should help in the clinical management of multiple pathologies accessible by OCT, it currently is hampered by the overamplification of noise at high depth. Specifically, this refers to overamplification of noise in the deeper portion of the image, hereby referred to as the "overamplified area" (OVA). In particular, the OVA limits our ability to distinguish clearly the interface between the posterior limit of the "LC signal" and the commencement of the postlaminar region. An ability to measure reliably the full depth of the LC signal, assumed to equate to the distance between the anterior to posterior LC surfaces, will be important in helping us understand pathologic mechanisms affecting the optic nerve head.[22] Specifically, it will further our efforts towards the characterization of tissue biomechanics in glaucoma.[18–22]

In our study, we proposed a novel and adaptive compensation algorithm that can significantly reduce the overamplification of noise at high depth. This algorithm has a great potential to help increase the reliability of detecting the posterior LC boundary.

Materials and Methods

The aim of our study was to develop a novel and improved compensation algorithm that can enhance the visibility of the full depth of the LC signal (anterior and posterior surfaces) in OCT images of the human ONH. In the following sections, we briefly describe the existing compensation algorithms for OCT applications and highlight their limitations. We then present an improved algorithm, which we refer to as "adaptive compensation." The performance of this algorithm then is assessed using OCT images of the ONH obtained from three human subjects.

Current Limitations of OCT-Based Compensation

Our current compensation algorithms,[10,21] when applied to OCT images of the human ONH, significantly improved the visibility of the peripapillary sclera and LC, but at the cost of increased and amplified noise in the deepest part of the compensated image (Fig. 1). Our compensation model stated that the pixel intensity of an A-Scan $I_{i,j}$ is modified (compensated), such that:

$$I_{i,j}^{comp} = \underbrace{\frac{1}{2\sum_{k=i}^{N} I_{k,j}^{n}}}_{\text{Compensation Factor}} \times I_{i,j}^{n} \qquad (1)$$

where i is the A-Scan pixel number ranging from *1* (top of the image) to N (bottom of the image) for a given A-Scan j, and n is an exponent that will increase image contrast when it is superior to 1. According to such a model, pixel intensity values located in the upper part of the image are multiplied by a small compensation factor, while those in the deeper part of the image (low signal) are multiplied by a large compensation factor. Therefore, such a compensation model is designed to restore signal loss and does so despite the limitations of the acquisition system. As such, when the signal is very weak (e.g., due to excessive attenuation), the algorithm still will attempt to compensate and will apply a large compensation factor to the noise. This results in an overamplification of noise in deeper tissue layers. As the LC usually is located in the deeper part of an OCT ONH B-Scan, the overamplification of "deeper" noise limits our ability to detect the posterior LC boundary adequately.

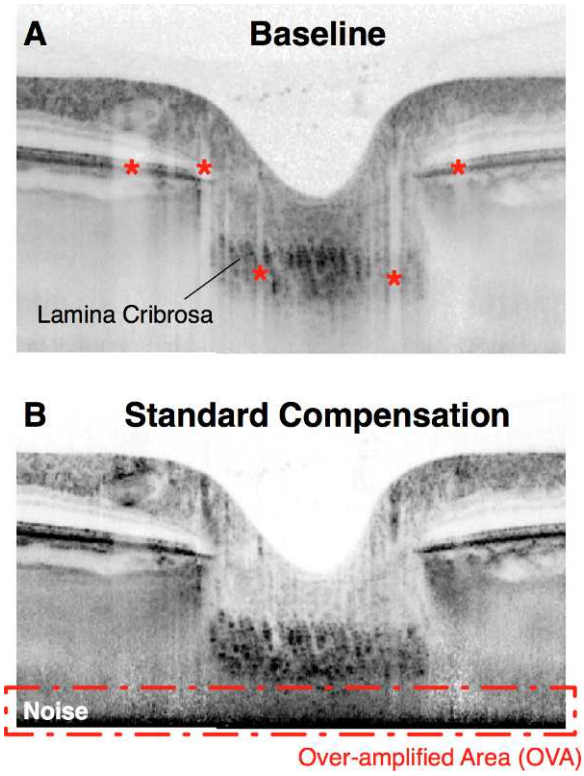

Figure 1. (**A**) Baseline OCT image of a subject's ONH. (**B**) Standard compensation was applied to the baseline image to remove blood vessel shadows (indicated by *red asterisks*), enhance contrast, and improve visibility of the deep tissue layers. However, standard compensation is hampered by noise amplification at the bottom of the compensated image (as shown in the OVA delineated in *dash-dotted red*).

Adaptive Compensation

To remove noise overamplification, and thus improve the performance of the compensation operation, we developed an adaptive compensation algorithm. The key operation controls noise overamplification by preventing the denominator of the compensation factor (Equation 1) to decrease further once the information in the more superficial regions has been compensated and the remaining signal (pixel intensity) of the deeper regions is pure noise.

The first and simplest approach is to add a constant term to the denominator to prevent it from reaching near-zero values. However, such an approach also would affect all compensation estimates within OCT A-Scans, including those of interest within the tissues, thereby progressively decreasing the quality of the compensation.

A second approach is to perform compensation by applying Equation 1 until the original OCT signal is brought below a predetermined threshold, after which the compensation factor is kept constant (Fig. 2C). This is an attractive solution when noise levels in the deeper regions are very small, especially when OCT signal averaging has been performed during acquisition, and when noise overamplification only arises at the very bottom of the image. However, it is not possible simply to threshold the signals, as pixel intensity can vary widely between A-Scans and from one OCT acquisition to the next. Furthermore, the "weak" signal is precisely the issue caused by attenuation that we are trying to address.

The third potential approach is "adaptive compensation." As detailed in our previous report,[10] the OCT device transmits a light beam that is attenuated progressively by the tissue layers; its energy decreases progressively until the scattered light is too weak to be detected by the OCT sensor. Therefore, in our approach, we

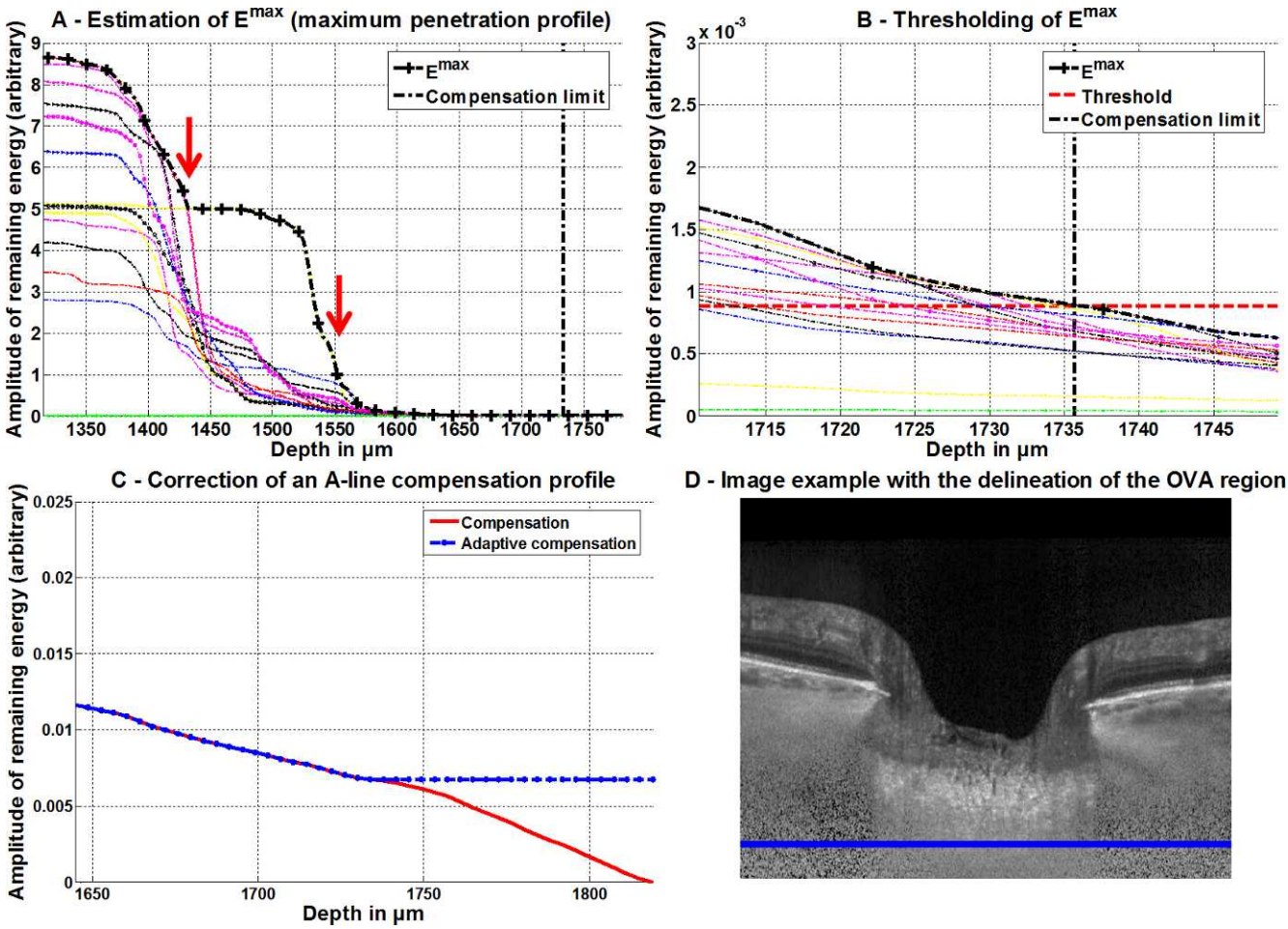

Figure 2. (**A**) Illustration of the computation of the penetration profile E^{max}, the maximum of all A-Scan intensity profiles plotted below the E^{max} curve as a function of depth (referenced from the *top* of the image). *Red arrows* points at locations where the remaining energy profiles from different A-Scans contribute clearly to the estimation of the penetration profile. (**B**) Zoom on (**A**) and details of the threshold (in *horizontal dashed line*) and of the corresponding compensation depth limit (*vertical dash-dotted line*). (**C**) Example of the remaining energy profile for a single A-Scan: when the energy threshold is reached, the compensation process is stopped and the data no longer are amplified. (**D**) Visualization of the compensation depth limit (*horizontal blue line*) obtained for the 0.1‰ energy threshold. In this adaptive compensation image, the OVA is defined below the depth limit (in *blue*) where no more than 0.1‰ of the energy remains and the compensation process is stopped to prevent overamplification.

considered applying a threshold to the remaining energy rather than to the original OCT signal. Indeed, thresholding the signal would remove many small values, which could, once compensated, reveal to be much larger than in the raw data. As these small values act in a cumulative manner in the compensation process, suppressing them potentially may risk impacting the final compensation estimates. Using our methodology, when an energy threshold is reached, the compensation factor is kept constant so as to maintain the stability of Equation 1 (Fig. 2C). For each pixel of each A-Scan, the remaining energy can be simply expressed as:

$$E_{i,j} = \sum_{k=i}^{N} \left[I_{k,j}^{n} \right]^2 \quad (2)$$

where i is the OCT pixel index for a given A-Scan j.

However, this approach cannot be applied for each A-Scan independently, since for OCT A-Scans affected by strong attenuation, the energy threshold will be reached too early (i.e., before reaching the bottom of the image). Therefore, the likelihood of the compensation algorithm "saving" potentially useful information in that region of the A-Scans would be limited. However, once all A-Scans have lost their energy, the compensation can be stopped safely for all A-Scans.

To avoid choosing the threshold manually for each A-Scan, or for each image, we proposed an adaptive solution. The remaining energy was computed for all A-Scans of a given image (see example profiles in Figs. 2A, 2B). The maximum remaining energy (which corresponds to the A-Scan exhibiting the least attenuation) then is computed as:

$$E_i^{max} = \max_j \left[E_{i,j} \right] \quad (3)$$

This remaining energy profile, indicating the maximum penetration profile, then is used for thresholding, to determine the depth at which the compensation factor is kept constant, which then is used for all A-Scans (Fig. 2D). This approach avoids stopping the compensation prematurely in regions of strong attenuation, as it determines the limit from the A-Scans with smaller attenuation. We will describe the determination of an optimal threshold after acquisition and characterization of human OCT ONH images in the following sections.

Application and Image Selection

We note that adaptive compensation is aimed to work with any OCT devices or with any scan parameters. For the purpose of our work, we tested adaptive compensation with a commercially available device

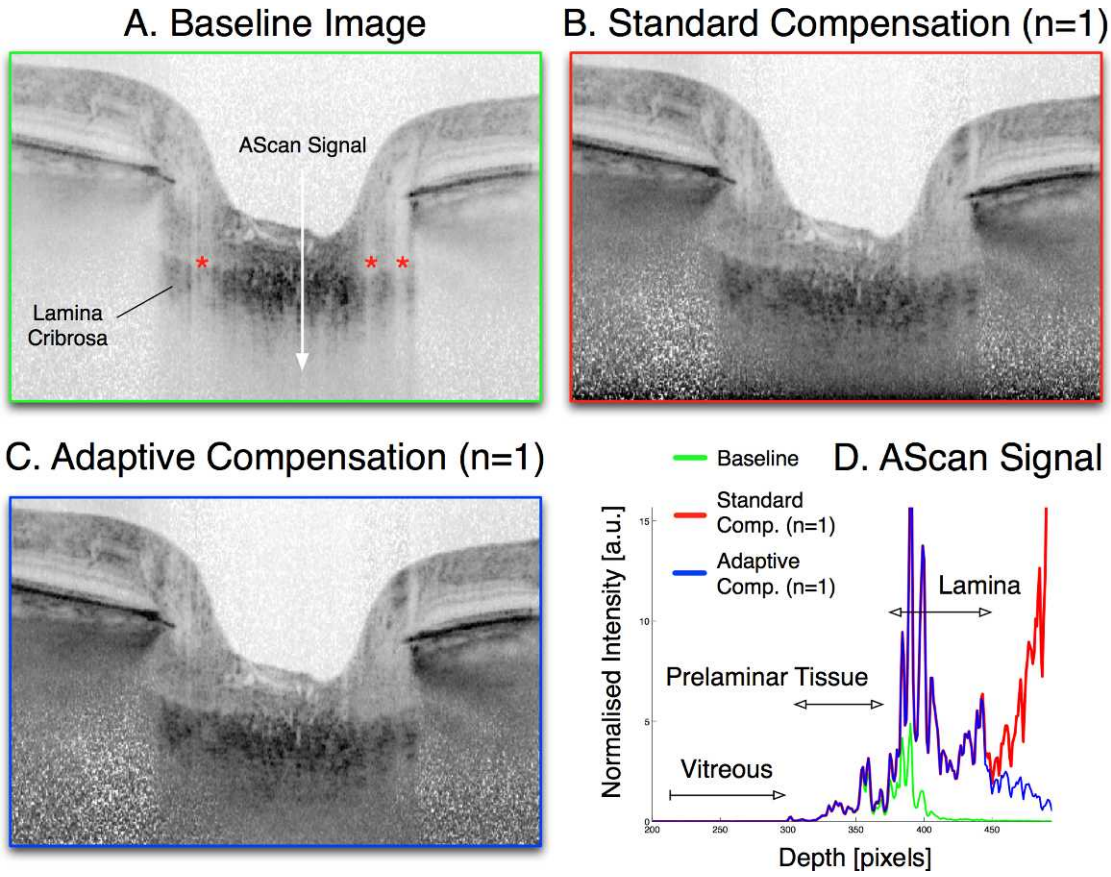

Figure 3. (**A**) Baseline OCT image of a healthy ONH (Subject 1). The LC is only partially visible. Note the presence of shadows as indicated by *red asterisks*. (**B**) Standard compensation was applied to the baseline image (exponent $n = 1$). Note that shadows are removed, and the LC becomes more uniform. However, noise is overamplified at high-depth which limits visibility of the posterior LC surface. (**C**) Adaptive compensation was applied to the baseline image ($n = 1$) to remove noise overamplification at high depth. (**D**) A-Scan signals (pixel intensity versus depth; see [**A**] for location) are shown for all three images. The baseline signal deteriorates rapidly in the LC region due to light attenuation. The standard compensation signal is recovered in the LC region, but degenerates rapidly due to noise overamplification beyond the posterior LC. The adaptive compensation signal is recovered within the LC, but does not exhibit noise overamplification beyond the posterior LC, thereby demonstrating optimal performance.

(Spectralis; Heidelberg Engineering, Heidelberg, Germany). Using such a device, spectral domain OCT volume scans were acquired from one eye of 4 healthy and 1 glaucoma human subjects (subject 1: healthy, male, 63 years, optical refraction −1.50/+1.00 diopters [D] × 2°, axial length 23.95 mm; subject 2: healthy, male, 34 years, optical refraction −3.00/+0.75 D × 90°, axial length 24.87 mm; subject 3: glaucoma, female, 77 years, optical refraction: +1.25/+0.50 D × 112°, axial length 22.99 mm; subject 4: healthy, male, 36 years, optical refraction −8.75/+2.00 D × 10°; axial length 26.99 mm; subject 5: healthy, male, 30 years, optical refraction: −2.00/+0.75 × 60°, axial length 24.81 mm). Imaging was performed at the New York Eye and Ear Infirmary, New York, NY (subjects 1–3) and at Moorfields Eye Hospital, London, UK (subjects 4 and 5), where regional ethics committee approval was obtained. All subjects gave informed consent and were treated in accordance with the tenets of the Declaration of Helsinki. Each volume scan comprised of 70 to 100 vertical (subjects 1–3) or horizontal (subjects 4 and 5) B-Scans acquired over a 15° × 15° retinal window, 768 A-Scans (of 496 pixels each) per B-Scan; each B-Scan was averaged 20 times for speckle noise reduction.

OCT volumes were chosen when the LC was partially visible (baseline images). Standard and adaptive compensation algorithms were applied to the central horizontal or vertical B-Scan of the right ONH of each subject.

Energy Threshold Selection

We aimed to select an appropriate energy threshold value for our adaptive algorithm. Such a value was estimated manually using the same set of OCT images described above. Note that these images were acquired in conditions that respected the assumptions of the model (i.e., full attenuation of the signal in the deep tissues as shown in Fig. 3).[10] The region of full-attenuation (which encompasses the OVA) was identified by an experienced clinician (NGS) using uncompensated images and images compensated using our standard algorithm, and its energy (sum of squared pixel intensity values from the baseline image) was computed. Then, the energy ratio (full-attenuation region versus entire image) was computed for all images to estimate the order of magnitude of the energy threshold to be used in the adaptive compensation algorithm.

Adaptive Compensation Efficiency

To verify that the adaptive compensation algorithm can remove signal overamplification, we computed the intralayer contrast in the OVA. The intralayer contrast is a measure of pixel intensity uniformity that varies between 0 (uniform pixel intensity values) and 1 (strongly heterogeneous pixel intensity values).[10] In other words, a low intralayer contrast indicates uniformity of pixel intensities at the bottom of the image and that no extra noise is generated from the

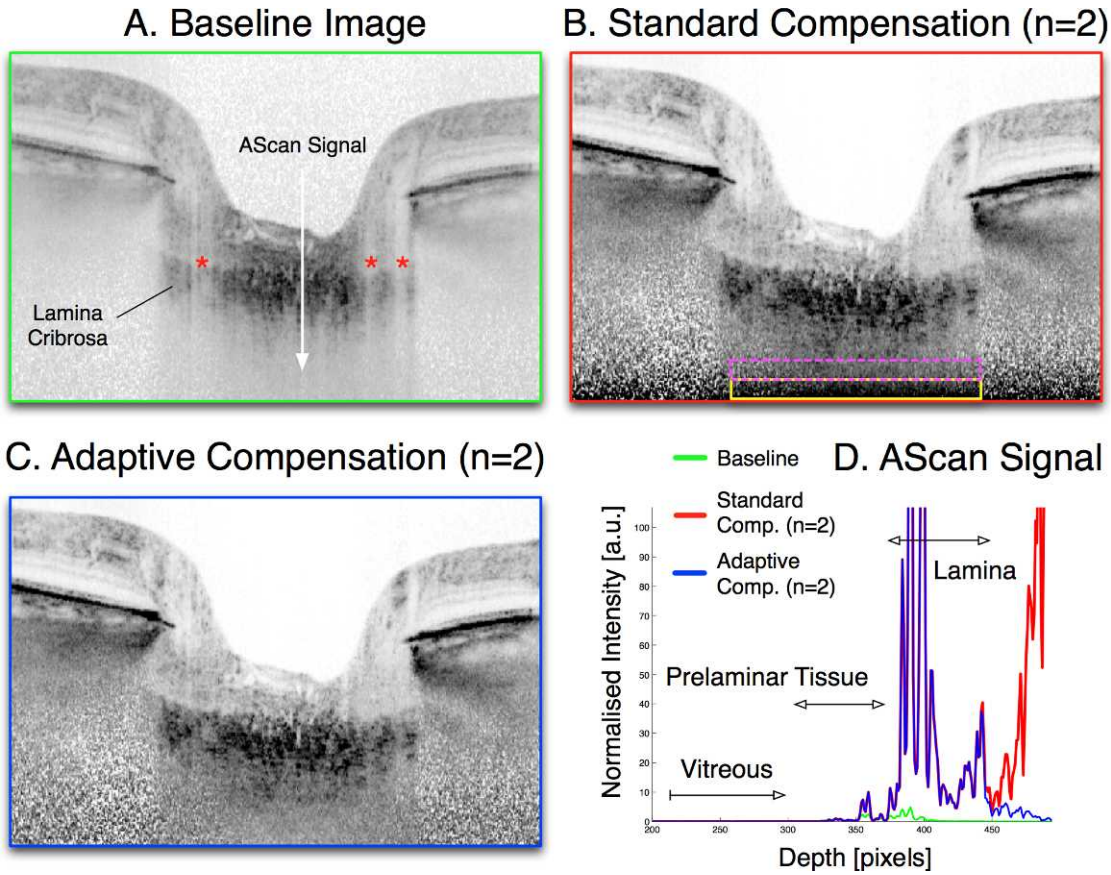

Figure 4. (**A**) Baseline OCT image of a healthy ONH (Subject 1). The LC is only partially visible. Note the presence of shadows as indicated by *red asterisks*. (**B**) Standard compensation was applied to the baseline image (exponent $n = 2$). Note that shadows are removed, and the LC becomes more uniform. However, noise is overamplified at high-depth, which limits visibility of the posterior LC surface. *Upper* and *lower* OVA regions (as defined to compute the intralayer contrasts) are shown in *pink* and *yellow*, respectively. (**C**) Adaptive compensation was applied to the baseline image ($n = 2$) to remove noise overamplification at high depth. (**D**) A-Scan signals (pixel intensity versus depth, see [**A**] for location) are shown for all three images. The baseline signal deteriorates rapidly in the LC region due to light attenuation. The standard compensation signal is recovered in the LC region, but this degenerates rapidly due to noise overamplification beyond the posterior LC. The adaptive compensation signal is recovered within the LC, but does not exhibit noise overamplification beyond the posterior LC, thereby demonstrating optimal performance.

compensation operation. Intralayer contrasts were computed between the upper and lower regions of the OVA (respectively, shown in pink and yellow for three of five subjects in Figs. 4–6; size of the regions of interest: 400×40 pixels) for all five subjects (for the uncompensated, standard compensation, and adaptive compensation images).

To verify that the adaptive compensation algorithm can improve detection of the putative posterior LC surface, we computed the interlayer contrast across the posterior LC boundary. The interlayer contrast is a measure of boundary detectability that varies between 0 (poorly detectable boundary) and 1 (highly detectable boundary).[10] Interlayer contrasts were computed between the region of the LC and that of the postlaminar tissues (size of the regions of interest 400×40 pixels) for all five subjects (for the uncompensated, standard compensation, and adaptive compensation images).

Effect of Energy Threshold Variations

To evaluate the impact of threshold selection, we increased the energy threshold by one, then by two orders of magnitude. Adaptive compensation was applied to all images for all threshold values and inter- and intralayer contrasts were computed as above.

Statistical Analyses

Intra- and interlayer contrasts are reported as mean ± SD. Statistical analyses were performed using unpaired Student's *t*-tests using Matlab (The Mathworks, Nattick, MA), with P values of less than 0.05 indicating statistical significance.

Results

Energy Threshold Selection

Energy ratios (full-attenuation region versus entire image) for all five subjects were 0.13‰ ± 0.09‰ (mean ± SD). This indicates that the potentially overamplified signals, which we assume are of no interest, represent less than about 0.2‰ of the energy of the image. Therefore, we selected a value of a similar order of magnitude, 0.1‰, as an appropriate energy threshold for our adaptive compensation algorithm.

Adaptive Compensation Application

When applied to OCT images, adaptive compensation was shown to remove signal overamplification at high depth, as demonstrated through visualization of the OCT images (Fig. 3A–C) and through visualization of the pixel intensity signals for a given A-Scan (Fig. 3D). Results remained consistent across all tested images even when a higher exponent was used ($n = 2$) for contrast enhancement (Figs. 4–6). Overall, the LC was

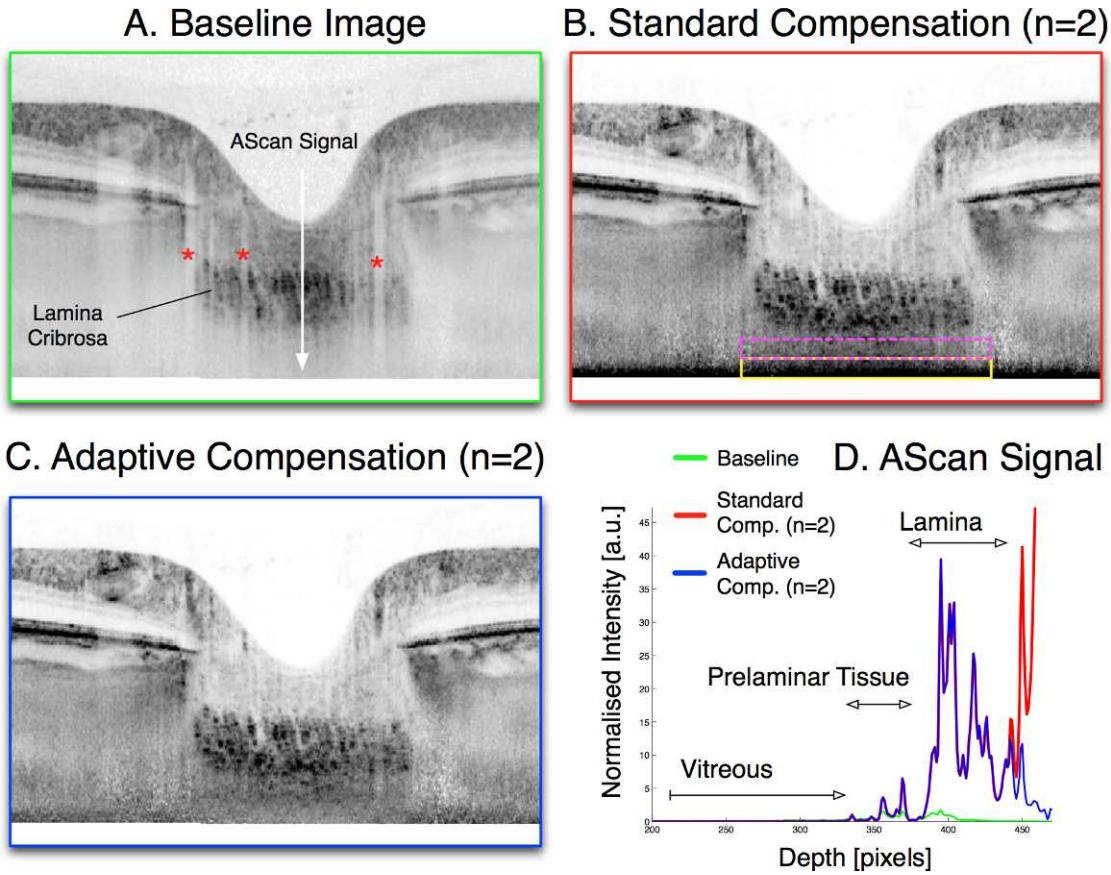

Figure 5. Adaptive compensation results for subject 2. The caption from Figure 4 also applies to this Figure.

better visualized and demarcated (or distinguished) following the application of the adaptive compensation algorithm.

Adaptive Compensation Efficiency

Intralayer contrasts in the OVA, computed for the uncompensated, standard compensation, and adaptive compensation images, are shown in Table 1 for all five subjects. Standard compensation significantly increased the intralayer contrasts from 0.30 ± 0.10 (uncompensated) to 0.62 ± 0.11 ($P < 0.001$) confirming that there was noise overamplification in the OVA. Adaptive compensation (threshold = 0.0001) significantly reduced intralayer contrasts from 0.62 ± 0.11 (standard compensation) to 0.30 ± 0.03 ($P < 0.001$). These results suggested that adaptive compensation outperforms standard compensation in terms of the reduction in noise overamplification.

Interlayer contrasts across the posterior LC boundary, computed for the uncompensated, standard compensation, and adaptive compensation images, are shown in Table 2 for all five subjects. Standard compensation significantly decreased the interlayer contrasts from 0.71 ± 0.12 (uncompensated) to 0.29 ± 0.13 ($P < 0.001$), suggesting that standard compensation led to poor detectability of the posterior LC boundary. Adaptive compensation (threshold = 0.1‰) significantly increased interlayer contrasts from 0.29 ± 0.13 (standard compensation) to 0.61 ± 0.21 ($P < 0.001$). This suggested that adaptive compensation has better performance than standard compensation in terms of posterior LC boundary detectability. Also, note that interlayer contrast values in the baseline images were artificially high simply due to light attenuation (i.e., signal decay with depth). Therefore, interlayer contrasts in the uncompensated image cannot be representative of posterior LC boundary visibility.

Effect of Energy Threshold Variations

Increasing the energy threshold in the adaptive compensation algorithm from 0.0001 to 0.001 or 0.01 led to a significant decrease in intralayer contrast from 0.30 ± 0.03 to 0.21 ± 0.08 ($P < 0.01$, Table 1). This also was significantly less than that of the baseline images (0.30 ± 0.10, $P < 0.05$, Table 1). Increasing the energy threshold also led to a significant increase in interlayer contrast from 0.61 ± 0.21 to 0.90 ± 0.06 ($P < 0.001$, Table 2). This was significantly higher than the "artificial values" from baseline images (0.71 ± 0.12, $P < 0.001$, Table 2). In other words, the highest energy threshold (0.01) appeared to provide the best performance in terms of removing noise overamplification and improving the detection of the posterior LC boundary, when adaptive compensation images were compared to baseline and standard compensation images. Adaptive compensation images for all energy thresholds and all subjects are shown in Figure 7. Note that other effects of compensation, such as blood vessel shadow removal, contrast enhancement, improved deep tissue visibility, and improved anterior LC boundary visibility, are maintained in the adaptive compensation algorithm.

Discussion

In our study, we proposed a novel adaptive compensation algorithm that can enhance the quality of OCT images of the ONH. This algorithm was aimed to overcome a limitation of

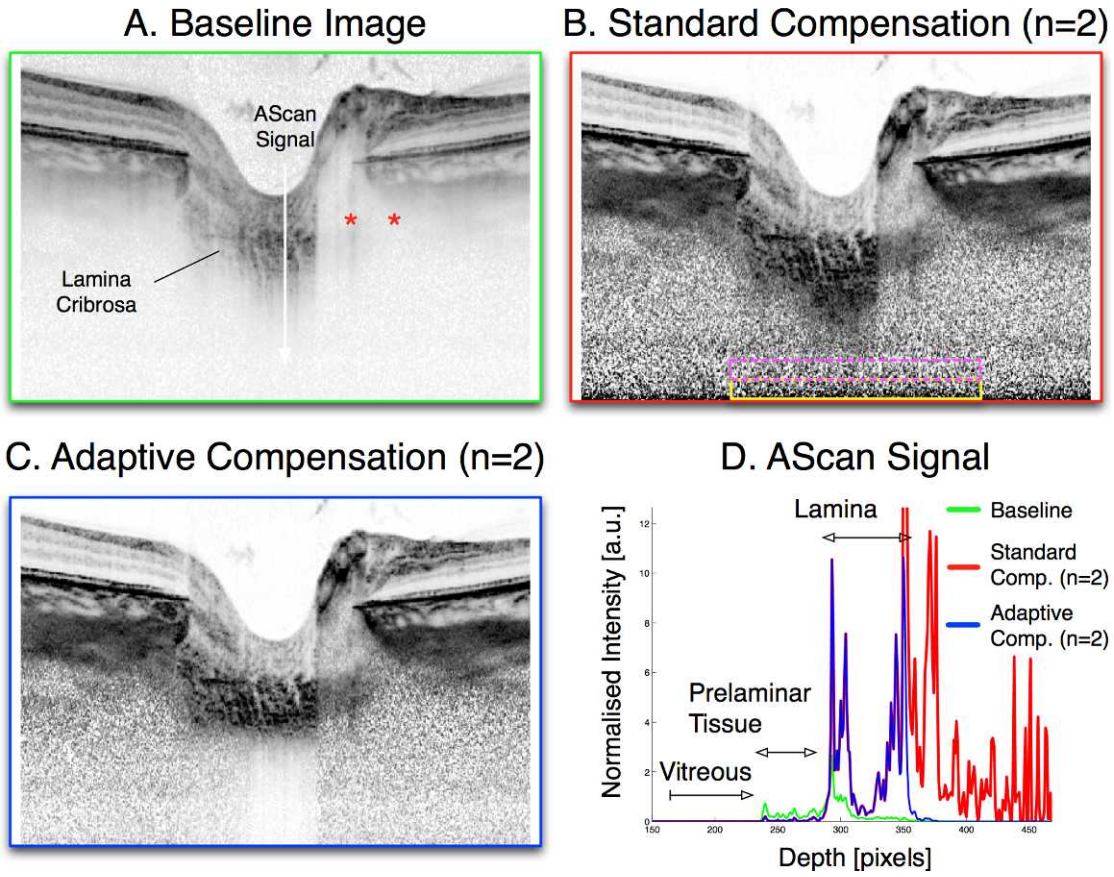

Figure 6. Adaptive compensation results for subject 4. The caption from Figure 4 also applies to this Figure.

our previously proposed compensation algorithm. Specifically, this algorithm was designed to improve our ability to detect and visualize the posterior LC boundary, a critical landmark that is believed to be of high importance in multiple optic neuropathies. Application of this algorithm may increase the likelihood that a reliable automated segmentation algorithm for detection of deep ONH tissues may be developed. Such an advance will assist greatly in our efforts to characterize the in vivo biomechanics of the ONH for glaucoma diagnosis, risk profiling, and management.[22–24]

Adaptive compensation was able to provide two major improvements compared to standard compensation. First, adaptive compensation successfully removed noise overamplification in the deep layers of the ONH (as demonstrated by the significant decrease in intralayer contrast in the OVA, Table 1, Fig. 7). Second, adaptive compensation was able to improve successfully the visibility of the posterior LC boundary (as demonstrated by the significant increase in interlayer contrast across the posterior LC boundary, Table 2, Fig. 7). It should be emphasized that these improvements were performed without compromising the characteristic features of compensation, such as contrast enhancement, blood vessel shadow removal, deep tissue visibility improvement, and anterior LC boundary visibility improvement. Therefore, we submit that adaptive compensation is superior to standard compensation.

It is important to note that the interlayer contrast values in the baseline images can appear to be large, and in some instances, they appeared larger than those computed in the

Table 1. The Intralayer Contrast (Upper versus Lower OVA) Was Computed for Two Different Images (Im 1 and 2) in Each of Five Subjects (Baseline, Standard Compensation, and Adaptive Compensation Images)

	Subject 1		Subject 2		Subject 3		Subject 4		Subject 5		
	Im 1	Im 2	Im 1	Im 2	Im 1	Im 2	Im 1	Im 2	Im 1	Im 2	Mean ± SD
Baseline image	0.34	0.31	0.34	0.33	0.23	0.22	0.44	0.40	0.19	0.18	0.30 ± 0.10
Standard compensation	0.67	0.64	0.56	0.50	0.48	0.46	0.72	0.71	0.72	0.74	0.62 ± 0.11
Adaptive compensation threshold = 0.0001	0.33	0.32	0.30	0.29	0.35	0.30	0.25	0.25	0.29	0.32	0.30 ± 0.03
Adaptive compensation threshold = 0.001	0.33	0.31	0.28	0.29	0.25	0.23	0.18	0.20	0.15	0.18	0.24 ± 0.06
Adaptive compensation threshold = 0.01	0.32	0.31	0.27	0.28	0.19	0.18	0.13	0.17	0.08	0.12	0.21 ± 0.08

Application of the standard compensation algorithm increased the intralayer contrast and, thus, increased signal overamplification at high depth. Application of the adaptive compensation algorithm reduced the intralayer contrast to levels lower than those observed in the baseline images. Therefore, adaptive compensation is able to remove signal overamplification at high depth.

Table 2. The Interlayer Contrast Was Computed across the Posterior LC Boundary for Two Different Images (Im 1 and 2) in Each of Five Subjects (Baseline, Standard Compensation, and Adaptive Compensation Images)

	Subject 1		Subject 2		Subject 3		Subject 4		Subject 5		
	Im 1	Im 2	Im 1	Im 2	Im 1	Im 2	Im 1	Im 2	Im 1	Im 2	Mean ± SD
Baseline image	0.82	0.85	0.80	0.81	0.50	0.55	0.69	0.75	0.66	0.67	0.71 ± 0.12
Standard compensation	0.37	0.35	0.10	0.12	0.24	0.30	0.25	0.28	0.48	0.45	0.29 ± 0.13
Adaptive compensation threshold = 0.0001	0.63	0.61	0.28	0.30	0.63	0.64	0.92	0.90	0.61	0.60	0.61 ± 0.21
Adaptive compensation threshold = 0.001	0.89	0.89	0.65	0.67	0.73	0.75	0.94	0.93	0.75	0.74	0.79 ± 0.11
Adaptive compensation threshold = 0.01	0.94	0.94	0.91	0.92	0.83	0.84	0.98	0.98	0.86	0.83	0.90 ± 0.06

Application of the standard compensation algorithm decreased the interlayer contrast and, thus, decreased the visibility of the posterior LC boundary. Application of the adaptive compensation algorithm increased the interlayer contrast to levels greater than those observed in the baseline images (higher threshold). Therefore, adaptive compensation is able to increase the visibility of the posterior LC surface.

adaptive compensated images (Table 2). They are, in fact, artificially large simply due to light attenuation (i.e., signal decay with depth). Therefore, interlayer contrasts in the baseline images cannot be representative of posterior LC boundary visibility.

In our study, we found that increasing the energy threshold to 10‰ in the adaptive compensation algorithm yielded the best performance (in terms of noise overamplification removal and posterior LC boundary visibility). While thresholds up to 1‰ appeared efficient, a lower value such as 0.1‰ was considered as a safe threshold (from energy calculations). Increasing the energy threshold above 1‰ could impact the LC signal. For example, in Figure 7, the LC appeared to thin as the threshold value increased. In practice, it will be important to control the accuracy of the proposed threshold (and confirm the fidelity of the posterior signal boundary to the true posterior LC surface) by comparing OCT images of the LC from human donor eyes with colocalized histologic cross-sections as has been undertaken previously in the monkey eye.[6] Such a calibration is critical to be able to generate valid and defensible in vivo LC thickness measurements using OCT.

Several limitations warrant further discussion. It is important to emphasize that we do not claim that we now are able to delineate exactly the posterior LC boundary using adaptive compensation. Many researchers identify the posterior limit of the signal "assumed" to be the LC as the posterior surface.[9,23–26] This assumption has been made without any direct comparison to human histology; the posterior LC surface was not found to be visible in an baseline OCT image of a normal monkey eye.[6] Part of the concern regarding "calling" the posterior surface is that it is not particularly easy to define histologically.[27] One approach, used in the comparison in the monkey eye, is to use a myelin stain to demarcate the posterior surface as myelination (usually) commences posterior to this. Structurally, there is a change in anisotropy whereby horizontal LC beams disappear to be replaced by vertical connective tissue septae.[28,29] The transition between the posterior part of the LC and the postlaminar region of the

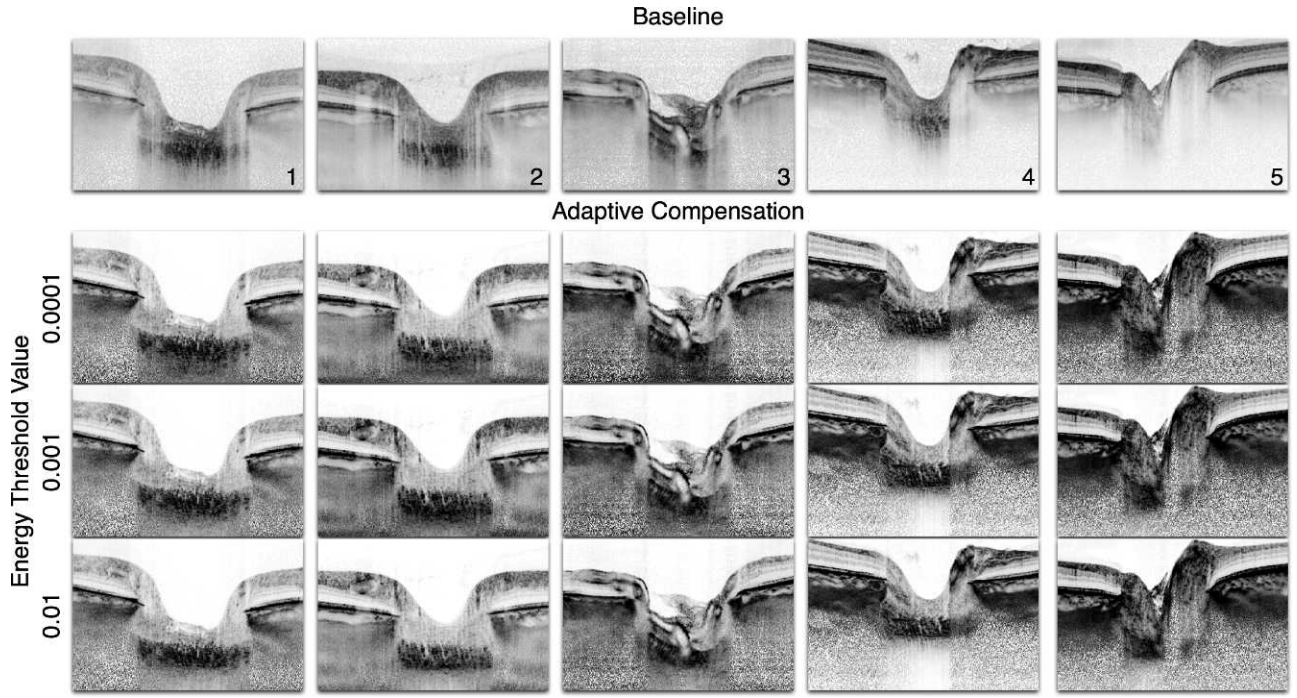

Figure 7. Adaptive compensation images are shown for the five tested subjects for three different energy threshold values (i.e., 0.1‰, 1‰, and 10‰). Increasing the energy threshold can improve reduce signal overamplification at high-depth and improve the visibility of the posterior LC boundary.

nerve head, therefore, is not necessarily "distinct" in histologic terms. While it may seem reasonable to assume that the posterior termination of lamina "signal" represents the posterior surface, we would recommend caution interpreting in vivo LC thickness measurements using OCT. This also can be illustrated by looking at the compensation results from subject 4 (Fig. 5), where adaptive compensation has removed what is believed to be postlaminar signal to visualize better the posterior LC boundary. This will need to be ascertained with further validation.

We have not applied our adaptive compensation algorithm to baseline images of the ONH in which the LC was felt to be nonvisible. It is unlikely that adaptive compensation will help visualize the posterior LC boundary if the LC signal is very weak to start with. Adaptive compensation is likely only to improve LC visibility in a proportion of subjects in which the LC is at least partly visible. The characteristics that define whether the LC is visible at all by OCT have yet to be identified to our knowledge.

As a final caveat, it is important to ensure that the images were acquired respecting the assumptions of the compensation model. In the situation where full signal attenuation is not observed in the deeper regions of the image, the compensation performance (standard or adaptive) will be altered. On the other hand, when full signal attenuation is observed below the LC signal in the baseline image, adaptive compensation will perform without compromising the visualization of the LC, as long as a small energy threshold (of the order of 0.1‰) is used.

In conclusion, we proposed an adaptive compensation algorithm that can improve the visibility of the LC in OCT images of the human ONH. This algorithm provided significant improvement compared to standard compensation by eliminating noise overamplification at high depth and improving the visibility of the posterior LC boundary. These improvements were performed while maintaining all other benefits of compensation, such as shadow removal and contrast enhancement.

References

1. Anderson DR. Probing the floor of the optic nerve head in glaucoma. *Ophthalmology*. 2012;119:1–2.
2. Park SC, Ritch R. High resolution in vivo imaging of the lamina cribrosa. *Saudi J Ophthalmology*. 2011;25:363–372.
3. Park SC, Kiumehr S, Teng CC, Tello C, Liebmann JM, Ritch R. Horizontal central ridge of the lamina cribrosa and regional differences in laminar insertion in healthy subjects. *Invest Ophthalmol Vis Sci*. 2012;53:1610–1616.
4. Park SC, De Moraes CG, Teng CC, Tello C, Liebmann JM, Ritch R. Enhanced depth imaging optical coherence tomography of deep optic nerve complex structures in glaucoma. *Ophthalmology*. 2012;119:3–9.
5. Lee EJ, Kim TW, Weinreb RN, et al. Three-dimensional evaluation of the lamina cribrosa using spectral-domain optical coherence tomography in glaucoma. *Invest Ophthalmol Vis Sci*. 2012;53:198–204.
6. Strouthidis NG, Grimm J, Williams GA, Cull GA, Wilson DJ, Burgoyne CF. A comparison of optic nerve head morphology viewed by spectral domain optical coherence tomography and by serial histology. *Invest Ophthalmol Vis Sci*. 2010;51:1464–1474.
7. Strouthidis NG, Fortune B, Yang H, Sigal IA, Burgoyne CF. Longitudinal change detected by spectral domain optical coherence tomography in the optic nerve head and peripapillary retina in experimental glaucoma. *Invest Ophthalmol Vis Sci*. 2012;52:1206–1219.
8. Kagemann L, Ishikawa H, Wollstein G, et al. Ultrahigh-resolution spectral domain optical coherence tomography imaging of the lamina cribrosa. *Ophthalmic Surg Lasers Imaging*. 2008;39:S126–S131.
9. Lee EJ, Kim TW, Weinreb RN. Reversal of lamina cribrosa displacement and thickness after trabeculectomy in glaucoma. *Ophthalmology*. 2012;119:1359–1366.
10. Girard MJ, Strouthidis NG, Ethier CR, Mari JM. Shadow removal and contrast enhancement in optical coherence tomography images of the human optic nerve head. *Invest Ophthalmol Vis Sci*. 2011;52:7738–7748.
11. Burgoyne CF, Downs JC, Bellezza AJ, Suh JK, Hart RT. The optic nerve head as a biomechanical structure: a new paradigm for understanding the role of IOP-related stress and strain in the pathophysiology of glaucomatous optic nerve head damage. *Prog Retin Eye Res*. 2005;24:39–73.
12. Albon J, Purslow PP, Karwatowski WS, Easty DL. Age related compliance of the lamina cribrosa in human eyes. *Br J Ophthalmol*. 2000;84:318–323.
13. Quigley HA, Addicks EM, Green WR, Maumenee AE. Optic nerve damage in human glaucoma. II. The site of injury and susceptibility to damage. *Arch Ophthalmol*. 1981;99:635–649.
14. Jonas JB, Berenshtein E, Holbach L. Lamina cribrosa thickness and spatial relationships between intraocular space and cerebrospinal fluid space in highly myopic eyes. *Invest Ophthalmol Vis Sci*. 2004;45:2660–2665.
15. Yang H, Thompson H, Roberts MD, Sigal IA, Downs JC, Burgoyne CF. Deformation of the early glaucomatous monkey optic nerve head connective tissue after acute IOP elevation in 3-D histomorphometric reconstructions. *Invest Ophthalmol Vis Sci*. 2011;52:345–363.
16. Kupersmith MJ, Sibony P, Mandel G, Durbin M, Kardon RH. Optical coherence tomography of the swollen optic nerve head: deformation of the peripapillary retinal pigment epithelium layer in papilledema. *Invest Ophthalmol Vis Sci*. 2011;52:6558–6564.
17. Heidary G, Rizzo JF III. Use of optical coherence tomography to evaluate papilledema and pseudopapilledema. *Semin Ophthalmol*. 2010;25:198–205.
18. Rebolleda G, Munoz-Negrete FJ. Follow-up of mild papilledema in idiopathic intracranial hypertension with optical coherence tomography. *Invest Ophthalmol Vis Sci*. 2009;50:5197–5200.
19. Hedges TR III, Vuong LN, Gonzalez-Garcia AO, Mendoza-Santiesteban CE, Amaro-Quierza ML. Subretinal fluid from anterior ischemic optic neuropathy demonstrated by optical coherence tomography. *Arch Ophthalmol*. 2008;126:812–815.
20. Contreras I, Noval S, Rebolleda G, Munoz-Negrete FJ. Follow-up of nonarteritic anterior ischemic optic neuropathy with optical coherence tomography. *Ophthalmology*. 2007;114:2338–2344.
21. Foin N, Mari JM, Davies JE, Di Mario C, Girard MJ. Imaging of coronary artery plaques using contrast-enhanced optical coherence tomography. *Eur Heart J Cardiovasc Imaging*. 2012;14:85.
22. Sigal IA, Ethier CR. Biomechanics of the optic nerve head. *Exp Eye Res*. 2009;88:799–807.
23. Park HY, Jeon SH, Park CK. Enhanced depth imaging detects lamina cribrosa thickness differences in normal tension glaucoma and primary open-angle glaucoma. *Ophthalmology*. 2012;119:10–20.
24. Lee EJ, Kim TW, Weinreb RN. Improved reproducibility in measuring the laminar thickness on enhanced depth imaging SD-OCT images using maximum intensity projection. *Invest Ophthalmol Vis Sci*. 2012;53:7576–7582.
25. Lee EJ, Kim TW, Weinreb RN, Suh MH, Kim H. Lamina cribrosa thickness is not correlated with central corneal thickness or axial length in healthy eyes: central corneal thickness, axial length, and lamina cribrosa thickness. *Graefes Arch Clin Exp Ophthalmol*. 2013;251:847–854.

26. Yang H, Qi J, Hardin C, et al. Spectral-domain optical coherence tomography enhanced depth imaging of the normal and glaucomatous nonhuman primate optic nerve head. *Invest Ophthalmol Vis Sci*. 2012;53:394–405.
27. Sigal IA, Flanagan JG, Lathrop KL, Tertinegg I, Bilonick R. Human lamina cribrosa insertion and age. *Invest Ophthalmol Vis Sci*. 2012;53:6870–6879.
28. Roberts MD, Hart RT, Liang Y, Bellezza AJ, Burgoyne CF, Downs JC. Continuum-level finite element modeling of the optic nerve head using a fabric tensor based description of the lamina cribrosa. Presented at the American Society of Mechanical Engineers (ASME) 2007 Bioengineering Conference; June 20–24, 2007; Keystone, CO.
29. Grytz R, Meschke G, Jonas JB. The collagen fibril architecture in the lamina cribrosa and peripapillary sclera predicted by a computational remodeling approach. *Biomech Model Mechanobiol*. 2011;10:371–382.